A Single-Stage Inductive-Power-Transfer Converter For Constant-Power and Maximum-Efficiency Battery Charging

Zhicong Huang, *Member, IEEE,* Chi-Seng Lam, *Senior Member, IEEE,* Pui-In Mak, *Fellow, IEEE,* Rui P. Martins, *Fellow, IEEE,* Siu-Chung Wong, *Senior Member, IEEE,* and Chi K. Tse, *Fellow, IEEE*

Abstract—This paper proposes a single-stage inductive-power-transfer (IPT) converter operating as a wireless constant-power (CP) and maximum-efficiency battery charger. By maintaining a constant output power rather than providing a constant output current throughout the dominant stage of battery charging, the IPT converter can make the utmost of its power capability, thus having a faster charging rate. The proposed single-stage IPT converter adopts series-series compensation and includes a switched-controlled capacitor (SCC) and a semi-active rectifier (SAR) in the secondary side. Manipulating the SCC and the SAR to emulate the optimum impedance of the resonator and the load, we propose a novel operation approach combining the merits of load-independent transfer characteristic and load impedance matching, to achieve a simple solution to CP charging and maximum efficiency throughout the charging process. Since the control scheme is based on fixed operating frequency and secondary-side real-time regulation, wireless feedback communication is not required. Moreover, soft switching and low voltage stress can be easily achieved in this IPT converter.

Index Terms—Inductive power transfer, battery charging, constant-power, maximum efficiency, soft switching.

I. INTRODUCTION

Inductive power transfer (IPT) is a growing technology to wirelessly supply power in applications where physical connection is inconvenient or impossible, e.g., hostile environments being affected by dirt and moisture [1], [2]. Typically, with abilities to simplify charging operation and remove safety concerns associated with electrical connection, IPT converters are suitable for wireless battery charging in a variety of scenarios, such as mobile electronics, biomedical implants, small home appliances and electric vehicles [3]–[8].

Constant current (CC) charging is a common charging technique and a dominant charging process for widely-used lithium-ion batteries [9]–[11]. As shown by the vertical CC line in Fig. 1, the charging current is kept constant, while the charging voltage is clamped to the terminal voltage of the battery and increases during charging. It can be observed that the charging power is started with a minimum value and increased to a maximum value at the completion of CC charging. Since charging at a high power level only lasts for a short duration, the power capacity of the charger has low utilization. Alternatively, to make the utmost of the power capability, the charger can control the output power to a predetermined maximum value and provide a constant-power (CP) charging for the battery [12]–[14]. As shown by the CP curve in Fig. 1, the charging current should be allowed to vary inversely with respect to the terminal voltage of the battery to maintain the desired CP charging. Obviously, given
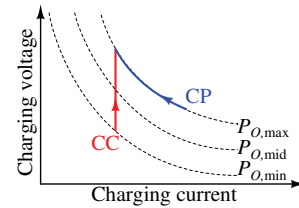

Fig. 1. V-I characteristics of CC charging and CP charging.

an identical maximum charging power, CP charging provides a faster charging speed than that of CC charging.

For a conductive charger, it is relatively easy to facilitate CP charging in its battery management system, which operates the charger as a current source, constantly varying according to the charging power profile [14]–[16]. However, to our best knowledge, IPT converters with the ability of wireless CP charging are seldom explored in literature, which motivates us to investigate the feasibility of wireless CP charger. In general, an IPT converter should be designed to operate at some fixed operating frequencies with load-independent transfer characteristic for minimal control complexity and operate within a restricted load range to achieve maximum efficiency [17]–[19]. However, only constant current or constant voltage output is achievable at these fixed operating frequencies that the output power of the IPT converter is determined by the load condition and cannot comply with the CP charging profile [20], [21]. An intuitive idea for CP output is using a two-stage IPT system, where a front-end converter can be used to modulate the input amplitude of the IPT converter or a load-side converter can be cascaded to the IPT converter for power regulation [22]–[25]. Due to the extra power stage, penalties of power loss, control complexity and/or wireless feedback communication are inevitable. Moreover, keeping single-stage design in mind, the IPT converter should also have load matching ability to achieve high efficiency. Otherwise, the efficiency significantly degrades at some mismatched loading conditions [26]–[28]. Since the load range during battery charging is normally wide, it is difficult for a single-stage IPT converter to maintain the maximum efficiency, while permitting fixed operating frequency, soft switching, no extra cascading converter, and no wireless feedback communication [28]. Therefore, it is challenging for an IPT converter to achieve the required output for CP charging and maintain the maximum efficiency throughout the charging process.

Aimed at filling the gap of wireless CP charging, this paper presents and explores a single-stage IPT converter
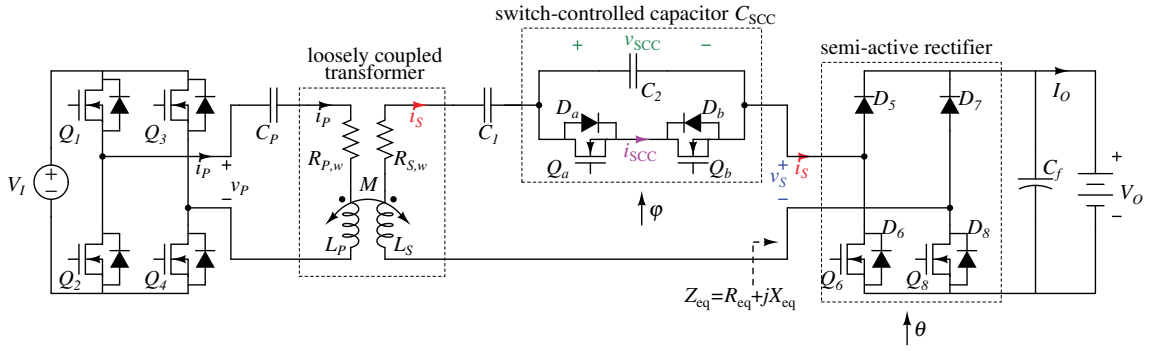
Fig. 2. Schematics of the proposed wireless CP charging system.

which adopts series-series compensation with a switched-controlled compensation capacitor (SCC) and a semi-active rectifier (SAR) in the secondary side. Combining the merits of load-independent transfer characteristic and load impedance matching, a novel operation approach is proposed for CP and maximum-efficiency charging. By controlling the SCC and the SAR, an optimum load and a constant secondary resonator current are maintained simultaneously, such that CP and maximum-efficiency charging can be simply implemented. The control scheme is based on fixed operating frequency and secondary-side real-time regulation, eliminating wireless feedback communication. Moreover, soft switching and low voltage stress can be easily achieved in this IPT converter.

II. PROPOSED WIRELESS CONSTANT-POWER BATTERY CHARGER

A. System Structure

Fig. 2 shows the proposed wireless CP battery charger based on a series-series compensated inductive power transfer (SSIPT) converter with a switched-controlled compensation capacitor (SCC) and a semi-active rectifier (SAR). In the schematic of the proposed system, the magnetic coupler has primary self inductance L_P, secondary self inductance L_S, and mutual inductance M. The coupling coefficient is defined as $k = \frac{M}{\sqrt{L_P L_S}}$. Coil losses in the primary and the secondary are represented by resistances $R_{P,w}$ and $R_{S,w}$, respectively. Both coils of the magnetic coupler are compensated by a capacitor in series connection. C_P is the primary compensation capacitor with fixed capacitance value, while a fixed-value capacitor C_1 as well as an SCC in series connection is used for secondary compensation with variable capacitance. The SCC consists of a fixed-value C_2 and two MOSFET switches Q_a and Q_b, with equivalent variable capacitance C_{SCC}. D_a and D_b are the anti-parallel body diodes of Q_a and Q_b, respectively. Compared with a single SCC, series connection of a fixed-value capacitor and an SCC can help to reduce the voltage stress of the SCC switches, which will be discussed in detail in Section IV-A. v_{SCC} is the voltage across the SCC, and i_{SCC} is the current flowing through the SCC. DC voltage source V_I is modulated into AC voltage v_P at an angular frequency ω to drive the primary coil by a full-bridge inverter with four MOSFET switches Q_1–Q_4. AC output is rectified to DC output by the
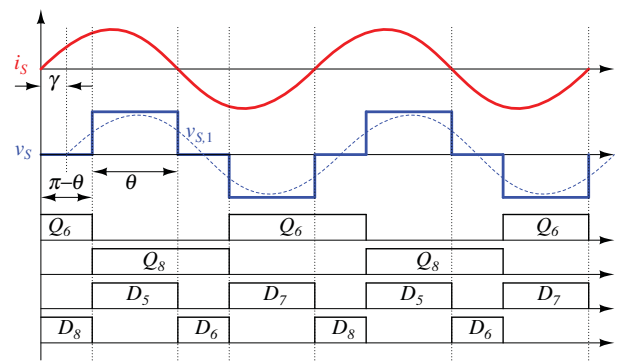

Fig. 3. Switching sequences and operating waveforms of the SAR.

semi-active rectifier (SAR) with output filter capacitor C_f. The SAR consists of two diodes D_5 and D_7 in the upper legs, and two MOSFET switches Q_6 and Q_8 in the lower legs. D_6 and D_8 are the anti-parallel body diodes of Q_6 and Q_8, respectively. Secondary AC voltage v_S and AC current i_S are the inputs of the SAR circuit. V_O and I_O are DC charging voltage and current for the battery, respectively.

B. Operation of the Semi-Active Rectifier

The switching sequences and the operating waveforms of the SAR are shown in Fig. 3. MOSFET switches Q_6 and Q_8 are turned on during the on-time of their anti-parallel diodes to have ZVS. Both Q_6 and Q_8 are turned on for half a cycle, and they are complements of each other. Therefore, Q_6 and Q_8 are turned off with a time delay of $\pi - \theta \in [0, \pi]$, to the zero-cross points of i_S. Thus, conduction angle θ of the SAR has a maximum π and minimum 0. It is noted that the change of θ will affect the phase angle between v_S and i_S. As shown in Fig. 3, $v_{S,1}$ is the fundamental component of v_S that it lags i_S with a phase angle given by $\gamma = \frac{\pi - \theta}{2}$. Therefore, the equivalent load is an impedance instead of the usual pure resistance [28], [29].

Since the battery charging is a slow process compared with the operating period of the SSIPT converter, the battery is modeled as a resistor determined by charging voltage and charging current, i.e., $R_L = \frac{V_O}{I_O}$. It has been studied that the
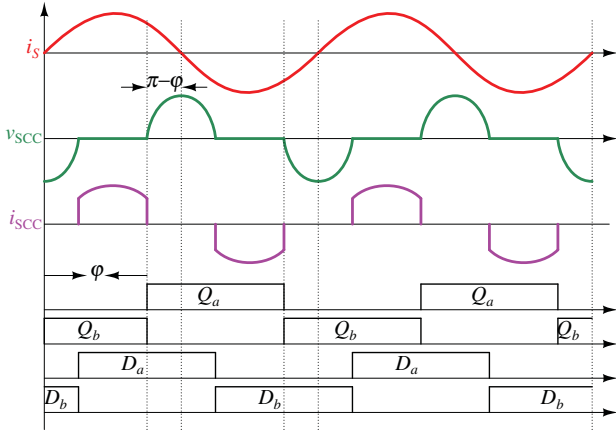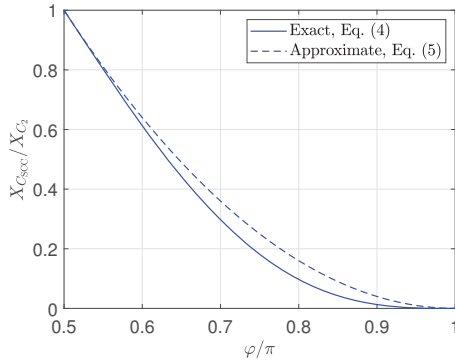
Fig. 4. Switching sequences and operating waveforms of the SCC.

Fig. 5. Equivalent impedance $X_{C_{\text{SCC}}}$ of the SCC versus control angle φ.

SAR together with the resistive load can be represented by an equivalent fundamental impedance [30], [31], given by

$$Z_{\text{eq}} = R_{\text{eq}} + jX_{\text{eq}}, \tag{1}$$

where

$$R_{\text{eq}} = \frac{8}{\pi^2} R_L \sin^4(\frac{\theta}{2}), \text{ and} \tag{2}$$

$$X_{\text{eq}} = -\frac{8}{\pi^2} R_L \sin^3(\frac{\theta}{2}) \cos(\frac{\theta}{2}) \tag{3}$$

are equivalent resistance and capacitive reactance, respectively.

C. Operation of the Switched-Controlled Capacitor

The switching sequences and the operating waveforms of the SCC are shown in Fig. 4. Driving signals of Q_a and Q_b are synchronized with i_S, and have a control angle $\varphi \in [\frac{\pi}{2}, \pi]$ to the zero-cross point of i_S. Both Q_a and Q_b are turned on for half a cycle, and they are complements of each other. Since Q_a and Q_b are turned on and off at zero voltage, soft switching can be achieved to minimize the switching losses. The available charging time (or discharging time) for C_2 in half a cycle is $\pi - \varphi$, which decreases with the increase of φ and results in a small equivalent root mean square (RMS) value of v_{SCC}. Consequently, the equivalent capacitance C_{SCC} of the SCC can be modulated by varying the control angle φ.
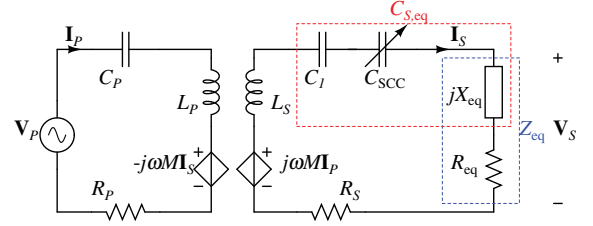

Fig. 6. AC equivalent circuit model of the proposed system.

It has been studied that C_{SCC} can be calculated by considering the fundamental components of i_S and v_{SCC} [32], [33]. The capacitive reactance donated by C_{SCC} is highlighted as

$$X_{C_{\text{CSS}}} = \left(2 - \frac{2\varphi - \sin 2\varphi}{\pi}\right) X_{C_2} \tag{4}$$

$$\approx \frac{4(\varphi - \pi)^2}{\pi^2} X_{C_2}, \tag{5}$$

where $X_{C_{\text{CSS}}} = -\frac{1}{\omega C_{\text{CSS}}}$ and $X_{C_2} = -\frac{1}{\omega C_2}$. The complex expression (4) can be simplified into (5) by using quadratic curve fitting. Fig. 5 shows the exact and approximate curves of $X_{C_{\text{CSS}}}$ versus the control angle φ. It can be observed that, $X_{C_{\text{CSS}}}$ can be modulated from a nominal reactance X_{C_2} to zero as φ is varied from 0.5π to π.

Unless specified otherwise in the rest of the paper, $X_{\text{subscript}}$ represents the reactance of the corresponding component indicated by its subscript.

D. Equivalent Circuit Model

An equivalent circuit model of the proposed system using the fundamental approximation is shown in Fig. 6. The simplification is sufficiently accurate for resonant circuits operating near the resonant frequency [17]–[19]. Here, the equivalent circuit model of the proposed system is similar to that of a conventional SSIPT converter, except that the secondary compensation capacitance is variable and the load is not purely resistive. The load is represented by an equivalent impedance Z_{eq} with resistance R_{eq} in series with reactance X_{eq}. Variables $\mathbf{V}_P$, $\mathbf{I}_P$, $\mathbf{V}_S$ and $\mathbf{I}_S$ are phasors of the fundamental components of v_P, i_P, v_S and i_S, respectively. Resistor R_P includes losses from the primary coil and the inverter, while resistor R_S includes losses from the secondary coil, the SCC and the SAR. Detailed calculation of R_P and R_S will be given in Section IV-B for loss analysis.

As shown in Fig. 6, C_1, C_{SCC} and X_{eq} donate capacitve reactances in the secondary, and they can be represented by an equivalent secondary compensation capacitance $C_{S,\text{eq}}$, with its reactance satisfying

$$X_{C_{S,\text{eq}}} = -\frac{1}{\omega C_{S,\text{eq}}} = X_{C_1} + X_{C_{\text{SCC}}} + X_{\text{eq}}. \tag{6}$$

Therefore, the equations for the circuit model in Fig. 6 are

$$(R_P + jX_{L_P} + jX_{C_P})\mathbf{I}_P - jX_M\mathbf{I}_S = \mathbf{V}_P, \tag{7}$$

$$-(R_S + R_{\text{eq}} + jX_{L_S} + jX_{C_{S,\text{eq}}})\mathbf{I}_S + jX_M\mathbf{I}_P = 0, \tag{8}$$
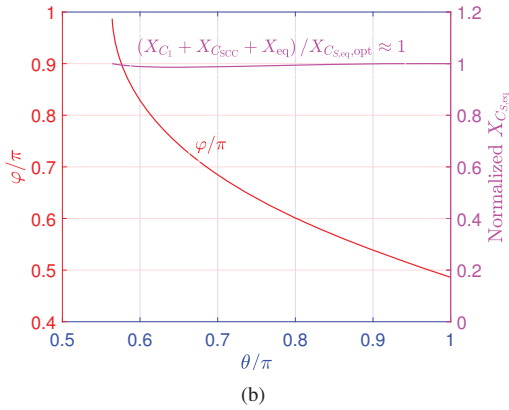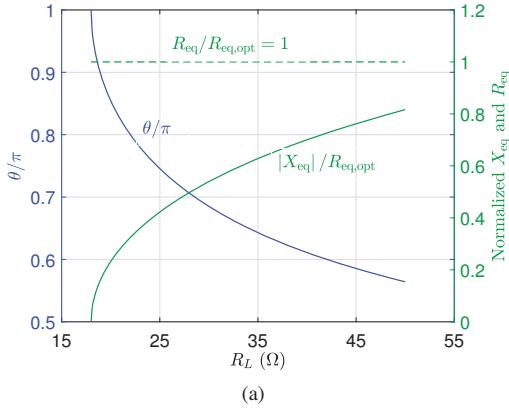
Fig. 7. (a) Conduction angle θ, normalized R_{eq}, normalized X_{eq} versus load resistance R_L. (b) Phase delay angle φ, normalized $X_{C_{S,\text{eq}}}$ versus conduction angle θ.

where $X_M = \omega M$, $X_{L_P} = \omega L_P$, $X_{C_P} = -\frac{1}{\omega C_P}$ and $X_{L_S} = \omega L_S$. The magnitudes of $\mathbf{V}_P$, $\mathbf{V}_S$ and $\mathbf{I}_S$ are given by

$$|\mathbf{V}_P| = \frac{4}{\pi} V_I, \tag{9}$$

$$|\mathbf{V}_S| = \frac{4}{\pi} \sin\left(\frac{\theta}{2}\right) V_O, \text{ and} \tag{10}$$

$$|\mathbf{I}_S| = \frac{\pi}{2} \frac{I_O}{\sin^2\left(\frac{\theta}{2}\right)}. \tag{11}$$

III. CONTROL SCHEME FOR CONSTANT-POWER AND MAXIMUM-EFFICIENCY CHARGING

A. Maximum Efficiency

Using the circuit model shown in Fig. 6, the efficiency can be calculated by

$$\eta = \frac{|\mathbf{I}_S|^2 R_{\text{eq}}}{|\mathbf{I}_S|^2 R_{\text{eq}} + |\mathbf{I}_S|^2 R_S + |\mathbf{I}_P|^2 R_P}$$
$$= \frac{X_M^2 R_{\text{eq}}}{[(R_{\text{eq}} + R_S)^2 + (X_{L_S} + X_{C_{S,\text{eq}}})^2] R_P + X_M^2 (R_{\text{eq}} + R_S)}. \tag{12}$$

Given a chosen operating frequency ω, the efficiency in (12) can be maximized as

$$\eta_{\text{max}} \approx \frac{1}{\frac{2}{\frac{X_M}{\sqrt{R_P R_S}}} + 1}, \text{ if} \tag{13}$$

Parameters	Symbols	Values
Self inductance	L_P, L_S	86 μH, 102 μH
Coupling coefficient	k	0.26
Coil resistance	$R_{P,w}$, $R_{S,w}$	0.3 Ω, 0.328 Ω
Inverter switch	$R_{\text{on}1}$	0.1 Ω
SCC switch	$R_{\text{on}2}$, $V_{\text{f}2}$	0.1 Ω, 0.7 V
SAR switch	$R_{\text{on}3}$, $V_{\text{f}3}$	0.1 Ω, 0.7 V
Operating frequency	$\frac{\omega}{2\pi}$	85 kHz
Compensation capacitance	C_P, C_1, C_2	40.8 nF, 44 nF, 166 nF
Optimum load resistance	$R_{\text{eq,opt}}$	fixed at 18 Ω

$$X_{L_S} + X_{C_{S,\text{eq}},\text{opt}} = 0, \text{ and} \tag{14}$$

$$R_{\text{eq,opt}} = X_M \sqrt{\frac{R_S}{R_P}}, \tag{15}$$

with the assumptions $\frac{X_M}{\sqrt{R_P R_S}} \gg 1$ and $\frac{R_{\text{eq}}}{R_S} \gg 1$. Variables $X_{C_{S,\text{eq}},\text{opt}}$ and $R_{\text{eq,opt}}$ are the optimum values of of $X_{C_{S,\text{eq}}}$ and R_{eq} leading to maximum efficiency, respectively.

From (15), the battery resistance R_L varying in a wide range, i.e., $R_L \in [R_{L,\text{min}}, R_{L,\text{max}}]$, should be transformed into a matched load resistance $R_{\text{eq,opt}}$ by the SAR. With (2) and (15), the conduction angle θ of the SAR is given by

$$\theta = 2 \arcsin\left(\sqrt[4]{\frac{R_{\text{eq,opt}}}{\frac{8}{\pi^2} R_L}}\right). \tag{16}$$

However, from (3), the change of θ also affects the load reactance X_{eq}, given by

$$X_{\text{eq}} = -R_{\text{eq,opt}} \cot\left(\frac{\theta}{2}\right). \tag{17}$$

In Fig. 7(a), the solid curve labeled with θ/π shows the change of θ with regard to R_L for optimum load resistance. Indicated by the dashed line, optimum load resistance $R_{\text{eq,opt}}$ can be achieved by controlling θ of the SAR. However, the magnitude of X_{eq} concurrently becomes larger with the decrease of θ, as shown in the solid curve labeled with $|X_{\text{eq}}|/R_{\text{eq,opt}}$. The simulation parameters are given in Table I and will be used for the rest of this paper unless specified otherwise.

To ensure (14), $C_{S,\text{eq}}$ should fully compensate L_S at the operating frequency that the equivalent capacitive reactance $X_{C_{S,\text{eq}}}$ should be constant at $X_{C_{S,\text{eq}},\text{opt}} = -X_{L_S}$. Therefore, the variation of $X_{C_{S,\text{eq}}}$ caused by X_{eq} should be offset by $X_{C_{\text{SCC}}}$. With (5), (6) and (17), the control angle φ of the SCC can be derived as

$$\varphi \approx \pi - \frac{\pi}{2} \sqrt{\frac{|X_{C_{S,\text{eq}},\text{opt}}| - |X_{C_1}| - |X_{\text{eq}}|}{|X_{C_2}|}}. \tag{18}$$

As shown in Fig. 7(b), with the coordinated control of φ with respect to θ given in red curve, $X_{C_{S,\text{eq}}}$ is almost constant at $X_{C_{S,\text{eq}},\text{opt}}$ achieving maximum efficiency given in magenta curve.

B. Constant-Power Charging

Equations (14) and (15) can be satisfied via controlling the conduction angle θ of the SAR and the control angle φ of the SCC, as discussed in Section III-A. As shown in
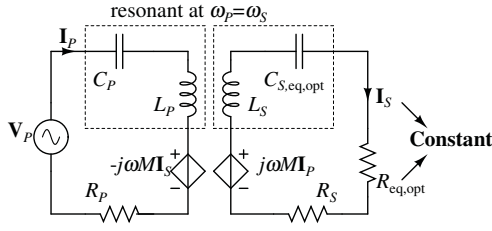
Fig. 8. Proposed operation approach to CP output and maximum efficiency with the merits of load-independent characteristic and load impedance matching.
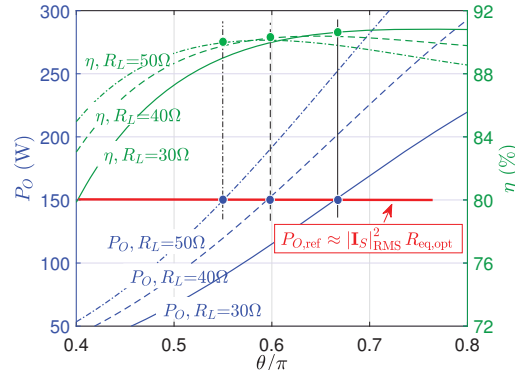

Fig. 9. Output power P_O and efficiency η versus conduction angle θ under different values of battery resistance R_L.

Fig. 8, with the controlled optimum load resistance $R_{\mathrm{eq,opt}}$ and null reactance in the secondary, i.e. $X_{L_S} + X_{C_{S,\mathrm{eq,opt}}} = 0$, the maximum efficiency given by (13) can be maintained over a wide range of battery resistance R_L. Besides, it has been widely studied that an SSIPT system can achieve load-independent output current, if operating with a null reactance in the primary [19]–[21]. Theoretically, if component losses are neglected, the magnitude of the load-independent output current i_S is highlighted as

$$|\mathbf{I}_S| \approx \frac{|\mathbf{V}_P|}{X_M}. \tag{19}$$

Therefore, with the merits of load-independent transfer characteristic and load impedance matching, a novel operation approach for CP output and maximum efficiency is proposed and illustrated as Fig. 8. The magnitude of the output current is constant at $|\mathbf{I}_S|$ due to the native load-independent current transfer characteristic [19]–[21], while the matching load for maximum efficiency is maintained constant at $R_{\mathrm{eq,opt}}$ via control. Therefore, given an input voltage, the proposed system outputs a constant output power at maximum efficiency, given by

$$P_{O,\mathrm{constant}} \approx |\mathbf{I}_S|^2_{\mathrm{RMS}} R_{\mathrm{eq,opt}}, \tag{20}$$

where subscript RMS represents the calculation of RMS value of corresponding variable.

With (9)-(11), (19) and (20), the charging power, DC charging voltage, DC charging current can be designed with

$$P_{O,\mathrm{constant}} = \frac{8}{\pi^2} \frac{V_I^2}{\omega M} \sqrt{\frac{R_S}{R_P}}, \tag{21}$$

$$V_O = \frac{V_I}{\sin^2(\frac{\theta}{2})} \sqrt{\frac{R_S}{R_P}}, \text{ and} \tag{22}$$

$$I_O = \frac{8}{\pi^2} \frac{V_I}{\omega M} \sin^2(\frac{\theta}{2}), \tag{23}$$

respectively.

C. Secondary Impedance Control Schemes

From (2), the equivalent load resistance R_{eq} can be modulated to the optimum value $R_{\mathrm{eq,opt}}$ by controlling the conduction angle θ. Assumed that the equivalent load impedance X_{eq} can be offset by the proper control of SCC impedance $X_{C_{\mathrm{SCC}}}$, the output power P_O is solely determined by the equivalent load resistance R_{eq}, given by $P_O \approx |\mathbf{I}_S|^2_{\mathrm{RMS}} R_{\mathrm{eq}}$. With (2), P_O takes a monotonic relationship with the control variable

θ. As an illustration, monotonic curves of P_O versus θ for various values of battery resistance R_L are shown in Fig. 9. It can be observed that, when P_O is constant at $P_{O,\mathrm{constant}}$ in (20), the proposed system operates at its optimized efficiency. Therefore, a simple PI controller can be used to achieve constant output power and maintain maximum efficiency, with $P_{O,\mathrm{constant}}$ in (20) being a control reference.

Fig. 10 shows the control diagram in practical implementation. Since the operating frequency in the primary is fixed, and only impedance control in the secondary is needed for constant power output and maximum efficiency, wireless feedback communication between the primary and the secondary can be eliminated. The charging voltage V_O and the charging current I_O are measured by sensors. P_O and R_L can be calculated by a multiplier and a divider, respectively. A simple PI controller applies the correction to the difference between P_O and $P_{O,\mathrm{ref}}$, and forms a control signal θ for the SAR. Meanwhile, with θ and R_L, another control signal φ is generated according to (18), or alternatively the measured relationship between φ and θ shown in Fig. 14. Zero crossing detection of i_S generates a synchronization signal for the PWM generations. Angles φ and θ are used to produce PWM driving signals for the SCC and the SAR, respectively.

IV. DESIGN CONSIDERATIONS

A. Minimizing Voltage Stress of the SCC

As analyzed in Section II-B and Section II-C, $|X_{\mathrm{eq}}|$ ranges from $|X_{\mathrm{eq}}|_{\mathrm{min}}$ to $|X_{\mathrm{eq}}|_{\mathrm{max}}$ depending on the battery resistance R_L, and $|X_{C_{\mathrm{SCC}}}|$ ranges from zero to $|X_{C_2}|$ with the control angle φ varying from π to 0.5π. Subscripts "max" and "min" represent the maximum and minimum values of corresponding variables, respectively. $X_{C_{\mathrm{SCC}}}$ can be controlled to offset the variation of X_{eq}, and thus $X_{C_{S,\mathrm{eq}}}$ can be constant at $X_{C_{S,\mathrm{eq,opt}}}$ to fully compensate X_{L_S}. From (14), design of C_1 should firstly ensure the requirements of full compensation in the secondary, as given by

$$|X_{C_1}| + |X_{C_2}| + |X_{\mathrm{eq}}|_{\mathrm{min}} \geq |X_{C_{S,\mathrm{eq,opt}}}|, \text{ and} \tag{24}$$

$$|X_{C_1}| + |X_{\mathrm{eq}}|_{\mathrm{max}} \leq |X_{C_{S,\mathrm{eq,opt}}}|. \tag{25}$$
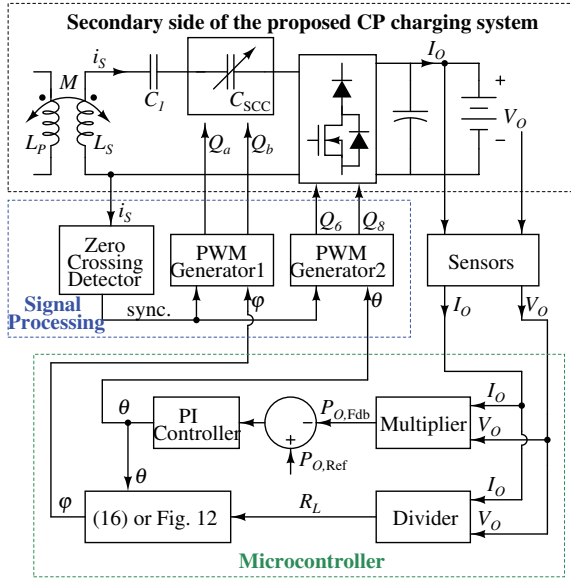
Fig. 10. Secondary impedance control diagram of the proposed CP charging system.

Fig. 11. Voltage stress $\left|\mathbf{V}_{\mathrm{SCC,max}}\right|$ of the SCC versus design value of X_{C_1}.

Fig. 12. Loss resistance ratio $\sqrt{\frac{R_S}{R_P}}$ and efficiency η versus equivalent battery resistance R_L.

The voltage stress of the SCC switches is determined by the maximum voltage across the SCC, as given by

$$|\mathbf{V}_{\mathrm{SCC,max}}| = |X_{C_2}| \, |\mathbf{I}_S| . \tag{26}$$

To reduce the voltage stress of the SCC switches, $|X_{C_2}|$ should be minimized. With (24), in other words, we should maximize $|X_{C_1}|$ in the design. With (25), the maximum value of $|X_{C_1}|$ can be derived as

$$|X_{C_1}|_{\mathrm{max}} = \left|X_{C_{S,\mathrm{eq}},\mathrm{opt}}\right| - |X_{\mathrm{eq}}|_{\mathrm{max}} . \tag{27}$$

The black curve in Fig. 11 shows the relationship between the voltage stress $\left|\mathbf{V}_{\mathrm{SCC,max}}\right|$ and the design value of $|X_{C_1}|$. It can be observed that, the voltage stress is significantly reduced by designing a large $|X_{C_1}|$.

Moreover, when the control angle is maximum, i.e., $\varphi = \pi$, $C_{S2,\mathrm{eq}}$ is shorten by the switches Q_a and Q_b, and thus maximum current stress of the SCC switches happens. Since i_S is constant as (19), maximum current stress of the SCC switches is given by

$$|\mathbf{I}_{\mathrm{SCC,max}}| = |\mathbf{I}_S| . \tag{28}$$

B. Loss Analysis

Theoretically, the proposed system operates with zero phase angle between the input voltage v_P and the input current i_P. In practice, the input impedance can be designed to be slightly inductive to facilitate ZVS of the MOSFET switches Q_1–Q_4 for switching loss reduction. A slight decrement of ω_P can fulfill the requirement and will not affect the output and the efficiency too much [20], [21]. Therefore, R_P representing the primary-side losses can be estimated by considering the primary-side coil resistance and the conduction losses of the inverter switches, given by

$$R_P = R_{P,w} + 2R_{\mathrm{on},1}, \tag{29}$$
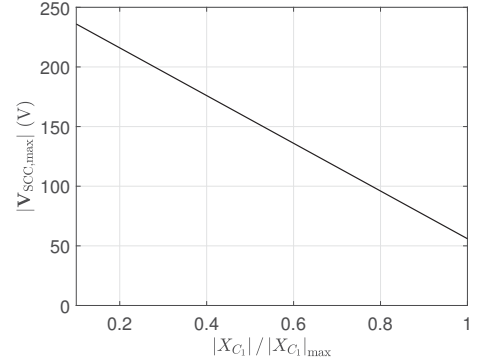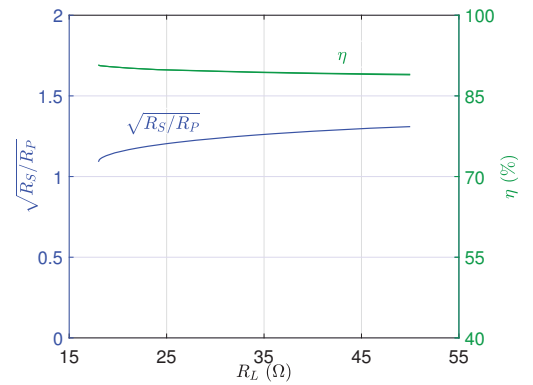
where $R_{\mathrm{on},1}$ is the conduction resistance of the inverter switches Q_1–Q_4. R_P can be considered as constant.

As analyzed in Section II-C, the SCC switches Q_a and Q_b are both soft switched. The conduction loss in the SCC switches can be estimated as

$$P_{\mathrm{SCC}} = I_{\mathrm{SCC,RMS}}^2 R_{\mathrm{on},2} + I_{\mathrm{SCC,avg}} V_{\mathrm{f},2}, \tag{30}$$

where $R_{\mathrm{on},2}$ and $V_{\mathrm{f},2}$ are the on-resistance and body-diode forward voltage of the MOSFET switches Q_a–Q_b, respectively. $I_{\mathrm{SCC,RMS}}$ and $I_{\mathrm{SCC,AV}}$ are the RMS value and average value of the current flowing through the SCC switches Q_a–Q_b, given by

$$I_{\mathrm{SCC,RMS}} = \sqrt{\frac{1}{\pi} \int_{\pi-\varphi}^{\varphi} (|\mathbf{I}_S| \sin x)^2 \, dx}, \text{ and} \tag{31}$$

$$I_{\mathrm{SCC,avg}} = \frac{1}{\pi} \int_{\pi-\varphi}^{\varphi} |\mathbf{I}_S| \sin x \, dx, \tag{32}$$

respectively.

Similarly, neglecting the small switching-off losses of Q_6 and Q_8, the conduction loss in the SAR can be estimated as

$$P_{\mathrm{SAR}} = i_{S,\mathrm{RMS}}^2 R_{\mathrm{on},3} + i_{S,\mathrm{avg}} V_{\mathrm{f},3}, \tag{33}$$

where $R_{\mathrm{on},3}$ is the on-resistance of the MOSFET switches Q_6 and Q_8, and $V_{\mathrm{f},3}$ is the forward voltage of the diodes D_5–D_8.

TABLE II
SYSTEM PARAMETERS

Battery Specifications		Values
Rated charging power P_O		150 W
Battery terminal voltage V_O		51–84.6 V

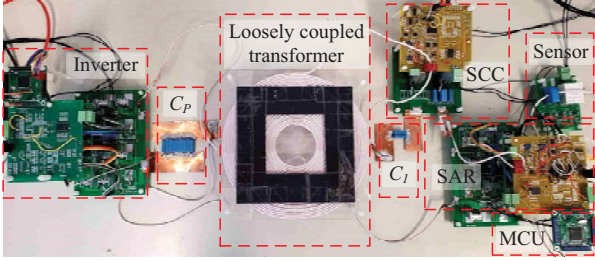| Parameters	Symbols	Measured Values
Input voltage	V_I	48 V
Switches	Q_1–Q_4, Q_a, Q_b, Q_6, Q_8	IPP60R099 with $R_{\mathrm{on}} \approx 0.099\ \Omega$ and $V_{\mathrm{F}} \approx 0.7$ V
Diodes	D_5, D_7	MBR20200 with $V_{\mathrm{F}} \approx 0.7$ V
Self inductance	L_P, L_S	85.09 μH, 101.13 μH
Coupling coefficient	k	0.262
Coil resistance	$R_{P,w}$, $R_{S,w}$	0.38 Ω, 0.41 Ω
Primary compensation	C_P	41 nF
Secondary compensation	C_1, C_2	155 nF, 55nF
Operating frequency	$\frac{\omega}{2\pi}$	85 kHz

Fig. 13. Experiment setup.

$i_{S,\mathrm{RMS}} = \frac{|\mathbf{I}_S|}{\sqrt{2}}$ and $I_{\mathrm{SAR,avg}} = \frac{2|\mathbf{I}_S|}{\pi}$ are the the RMS value and average value of i_S injecting into the SAR, respectively.

Incorporating the losses in the SCC and the SAR, equivalent series resistance R_S representing the losses in the secondary-side can be calculated as

$$R_S = R_{S,w} + \frac{P_{\mathrm{SCC}} + P_{\mathrm{SAR}}}{i_{S,\mathrm{RMS}}^2}. \qquad (34)$$

Loss resistance ratio $\sqrt{\frac{R_S}{R_P}}$ is simulated and shown by the blue curve in Fig. 12. Since the loss of the SCC increases with the increase of the control angle φ, $\sqrt{\frac{R_S}{R_P}}$ varies from 1.1 to 1.3 with respect to the battery resistance R_L. Theoretically, the optimum load resistance $R_{\mathrm{eq,opt}}$ should vary with the variation of $\sqrt{\frac{R_S}{R_P}}$. In practical, a slight deviation from the optimum load resistance will not affect the efficiency too much, and thus $R_{\mathrm{eq,opt}}$ can be fixed for simplicity. The simulated efficiency shown by the green curve in Fig. 12 slightly decreases mainly due to the increase of R_S. Nevertheless, the efficiency is approximately maintained maximum over the whole load range.

V. EXPERIMENTAL VERIFICATION

A. Specifications and Prototype

To verify the CP output and maximum-efficiency performance throughout the charging process, an experimental prototype is built, as shown in Fig. 13. The system parameters are given in Table II. According to the charging specifications,
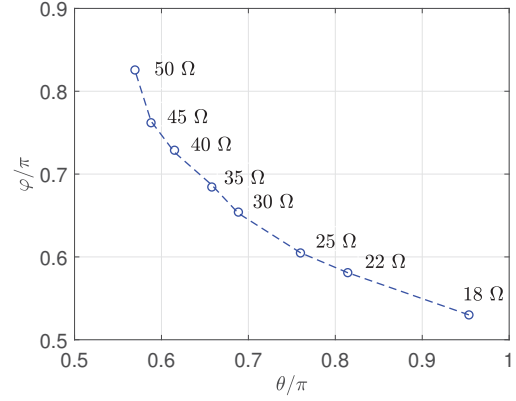

Fig. 14. Measured operating points at a constant output power of 147 W and the corresponding battery resistances.
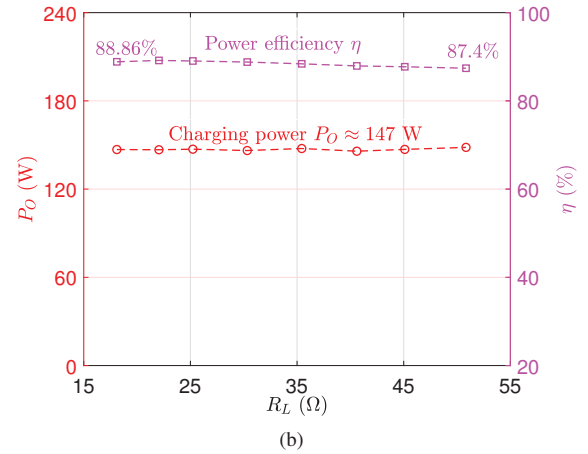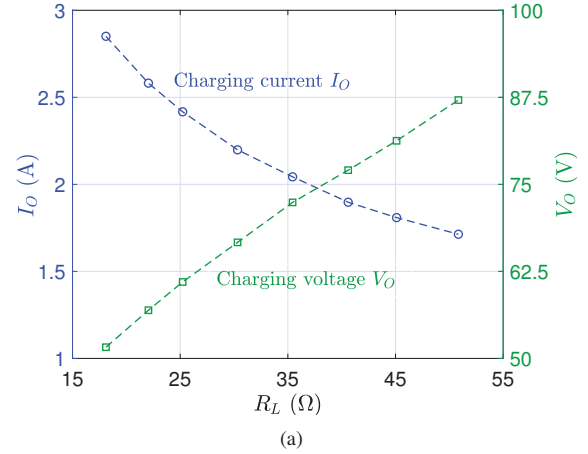

(a)

(b)

Fig. 15. (a) Measured output current and voltage versus battery resistance. (b) Measured power and efficiency versus battery resistance.

the equivalent battery resistance approximately ranges from 18 Ω to 50 Ω. An electronic load is used to emulate the battery. The input DC power and output DC power are measured by a Yokogawa WT1800 Precision Power Scope.

(a) $R_L = 18\ \Omega$
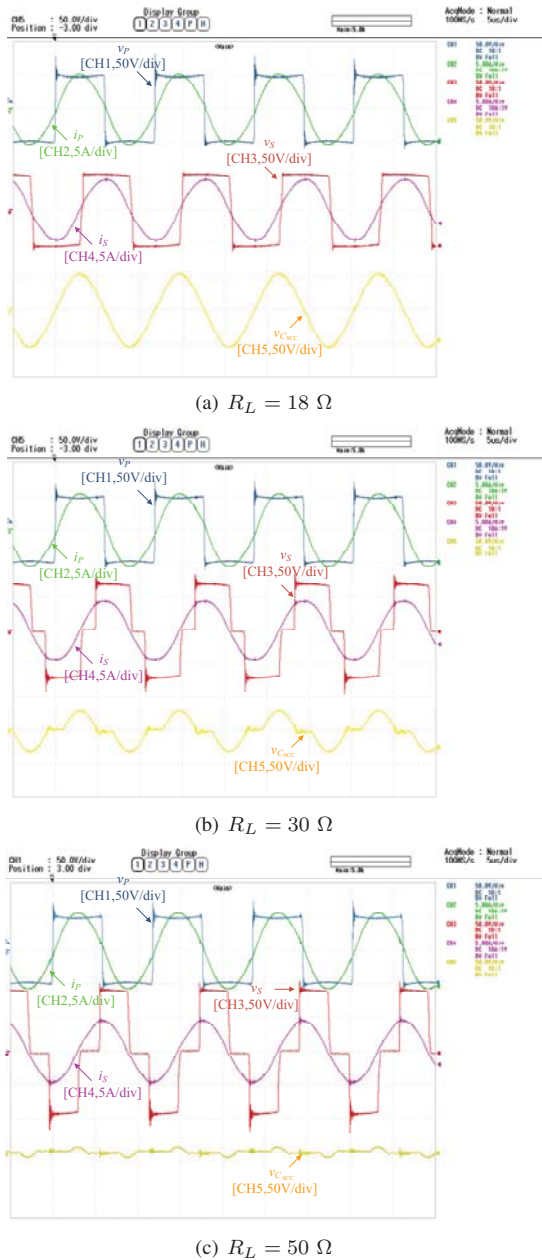

(b) $R_L = 30\ \Omega$

(c) $R_L = 50\ \Omega$

Fig. 16. Measured operating waveforms of the inverter, the SCC and the SAR at (a) the start (b) the middle and (c) the end of CP charging.

B. Measured Operating Points, Output Power and Efficiency

The operating frequency of the inverter is fixed at 85 kHz. Following the proposed operation approach in Section III, the conduction angle θ of the SAR and the control angle φ of the SCC are adjusted to achieve CP output and maintain maximum efficiency. The measured operating points (marked with "◯") are shown in Fig. 14, with φ and θ varying from 0.53π to 0.83π and from 0.95π to 0.57π, respectively.

The corresponding charging current (marked with "◯") varies inversely with respect to the charging output voltage (marked with "□") as shown in Fig. 15(a). The corresponding output power (marked with "◯") are approximately constant at 147 W, while a maximum efficiency (marked with "□")
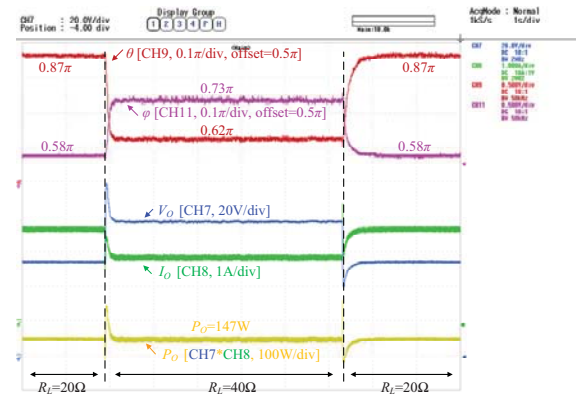

Fig. 17. Transient waveforms for R_L step changing from 20 Ω to 40 Ω and back to 20 Ω

is maintained at around 88% as shown in Fig. 15(a), which is consistent with the analysis in Section IV-B. To sum up, the proposed operation approach can ensure CP charging and maximum efficiency throughout the charging process.

Waveforms of the inverter, the SCC and the SAR are measured at the start, the middle and the end of CP charging, as shown in Fig. 16. ZVS is achievable in the inverter, the SCC and the SAR. The maximum voltage stress of the SCC switches is about 55 V as shown in Fig. 16(a), which coincides with the analysis in Section IV-A.

C. Transient Response Against Load Change

The closed-loop secondary impedance control scheme demonstrated in Section III-C is implemented in a microcontroller for CP charging and maximum efficiency throughout the charging process. Transient waveforms for step load changing are shown in Fig. 17. The output voltage V_O and output current I_O are measured and shown as CH7 in blue and CH8 in green, respectively. The control variables are observed from digital-to-analog outputs, where CH9 in red and CH11 in magenta represent the conduction angle θ of the SAR and the control angle φ of the SCC, respectively. P_O is calculated by multiplying V_O and I_O and shown the waveform in yellow. It can be observed that P_O is tightly regulated by direct control of θ, while φ is coordinately controlled with the variation of θ and R_L. No wireless communication is needed for the control of the proposed system.

VI. CONCLUSION

A single-stage IPT converter, which can operate as a wireless constant-power (CP) battery charger and maintain maximum efficiency throughout the charging process, is proposed in this paper. A novel operation approach combines the merits of load-independent transfer characteristic and load impedance matching, by controlling the control angle of the switch controlled capacitor and the conduction angle of the semi-active rectifier. The operating frequency of the IPT converter is fixed, and only a simple control in the secondary side is employed to achieve CP output and to ensure load matching for the maximum efficiency. No wireless feedback communication is

needed for the control, and all power switches realize zero-voltage-switching.

REFERENCES

[1] G. A. Covic and J. T. Boys, "Inductive power transfer," *Proc. IEEE,* vol. 101, no. 6, pp. 1276–1289, Jun. 2013.

[2] S. Lukic and Z. Pantic, "Cutting the cord: Static and dynamic inductive wireless charging of electric vehicles," *IEEE Electrific. Mag.,* vol. 1, no. 1, pp. 57–64, Sep. 2013.

[3] S. Y. R. Hui and W. W. C. Ho, "A new generation of universal contactless battery charging platform for portable consumer electronic equipment," *IEEE Trans. Power Electron.,* vol. 20, no. 3, pp. 620–627, May 2005.

[4] S. Y. Hui, "Planar wireless charging technology for portable electronic products and Qi," *Proc. IEEE,* vol. 101, no. 6, pp. 1290–1301, June 2013.

[5] Q. Chen, S. C. Wong, C. K. Tse and X. Ruan, "Analysis, design and control of a transcutaneous power regulator for artificial hearts," *IEEE Trans. Biomed. Circuits and Syst.,* vol. 3, no. 1, pp. 23–31, Feb. 2009.

[6] A. K. RamRakhyani, S. Mirabbasi and M. Chiao, "Design and optimization of resonance-based efficient wireless power delivery systems for biomedical implants," *IEEE Trans. Biomed. Circuits and Syst.,* vol. 5, no. 1, pp. 48–63, Feb. 2011.

[7] R. Bosshard and J. W. Kolar, "Inductive power transfer for electric vehicle charging: Technical challenges and tradeoffs," *IEEE Power Electron. Mag.,* vol. 3, no. 3, pp. 22–30, Sep. 2016.

[8] J. T. Boys and G. A. Covic, "The inductive power transfer story at the university of Auckland," *IEEE Circuits and Syst. Mag.,* vol. 15, no. 2, pp. 6–27, Apr. 2015.

[9] A. A. Hussein and I. Batarseh, "A review of charging algorithms for nickel and lithium battery chargers," *IEEE Trans. Veh. Technol.,* vol. 60, no. 3, pp. 830–838, Mar. 2011.

[10] J. Cao and A. Emadi, "A new battery/ultracapacitor hybrid energy storage system for electric, hybrid, and plug-in hybrid electric vehicles," *IEEE Trans. Power Electron.,* vol. 27, no. 1, pp. 122–132, Jan. 2012.

[11] M. Yilmaz and P. T. Krein, "Review of battery charger topologies, charging power levels, and infrastructure for plug-in electric and hybrid vehicles," *IEEE Trans. Power Electron.,* vol. 28, no. 5, pp. 2151–2169, May 2013.

[12] K. P. Dehnel, "Maximum power regulated battery charger," U.S. Patent 5382893, 1995.

[13] R. Tanikawa and H. Le, "Constant power battery charger," WO1996037941A1, 1996.

[14] N. K. Poon, B. M. H. Pong and C. K. Tse, "A constant-power battery charger with inherent soft switching and power factor correction," *IEEE Trans. Power Electron.,* vol. 18, no. 6, pp. 1262–1269, Nov. 2003.

[15] A. Kuperman, U. Levy, J. Goren, A. Zafransky and A. Savernin, "Battery charger for electric vehicle traction battery switch station," *IEEE Trans. Ind. Electron.,* vol. 60, no. 12, pp. 5391–5399, Dec. 2013.

[16] Y. Parvini, A. Vahidi and S. A. Fayazi, "Heuristic versus optimal charging of supercapacitors, lithium-ion, and lead-acid batteries: an efficiency point of view," *IEEE Trans. Control Syst. Technol.,* vol. 26, no. 1, pp. 167–180, Jan. 2018.

[17] W. Zhang, S. C.Wong, C. K. Tse, and Q. Chen, "Analysis and comparison of secondary series and parallel compensated inductive power transfer systems operating for optimal efficiency and load-independent voltage transfer ratio," *IEEE Trans. Power Electron.,* vol. 29, no. 6, pp. 2979–2990, Jun. 2014.

[18] Y. H. Sohn, B. H. Choi, E. S. Lee, G. C. Lim, G. H. Cho and C. T. Rim, "General unified analyses of two-capacitor inductive power transfer systems: equivalence of current-source SS and SP compensations," *IEEE Trans. Power Electron.,* vol. 30, no. 11, pp. 6030–6045, Nov. 2015.

[19] W. Zhang, S. C.Wong, C. K. Tse, and Q. Chen, "Load-independent duality of current and voltage outputs of a series or parallel compensated inductive power transfer converter with optimized efficiency," *IEEE J. Emerg. Sel. Topics. Power Electron.,* vol. 3, no. 1, pp. 137–146, Mar. 2015.

[20] Z. Huang, S. C. Wong and C. K. Tse, "Design of a single-stage inductive-power-transfer converter for efficient EV battery charging," *IEEE Trans. Veh. Technol.,* vol. 66, no. 7, pp. 5808–5821, Jul. 2017.

[21] X. Qu, W. Zhang, S. C. Wong and C. K. Tse, "Design of a current-source-output inductive power transfer LED lighting system," *IEEE J. Emerg. Sel. Topics Power Electron.,* vol. 3, no. 1, pp. 306–314, Mar. 2015.

[22] H. Zeng and F. Z. Peng, "SiC-based Z-source resonant converter with constant frequency and load regulation for EV wireless charger," *IEEE Trans. Power Electron.,* vol. 32, no. 11, pp. 8813–8822, Nov. 2017.

[23] O. Knecht and J. W. Kolar, "Performance evaluation of series-compensated IPT systems for transcutaneous energy transfer," *IEEE Trans. Power Electron.,* vol. 34, no. 1, pp. 438–451, Jan. 2019.

[24] A. Berger, M. Agostinelli, S. Vesti, J. A. Oliver, J. A. Cobos and M. Huemer, "A wireless charging system applying phase-shift and amplitude control to maximize efficiency and extractable power," *IEEE Trans. Power Electron.,* vol. 30, no. 11, pp. 6338–6348, Nov. 2015.

[25] Z. Li, C. Zhu, J. Jiang, K. Song and G. Wei, "A 3-kW wireless power transfer system for sightseeing car supercapacitor charge," *IEEE Trans. Power Electron.,* vol. 32, no. 5, pp. 3301–3316, May 2017.

[26] W. Zhong and S. Y. Hui, "Reconfigurable wireless power transfer systems with high energy efficiency over wide load range," *IEEE Trans. Power Electron.,* vol. 33, no. 7, pp. 6379–6390, Jul. 2018.

[27] W. X. Zhong and S. Y. R. Hui, "Maximum energy efficiency tracking for wireless power transfer systems," *IEEE Trans. Power Electron.,* vol. 30, no. 7, pp. 4025–4034, Jul. 2015.

[28] Z. Huang, S. C. Wong and C. K. Tse, "An inductive-power-transfer converter with high efficiency throughout battery-charging process," *IEEE Trans. Power Electron.,* vol. 34, no. 10, pp. 10245–10255, Oct. 2019.

[29] T. Diekhans and R. W. De Doncker, "A dual-side controlled inductive power transfer system optimized for large coupling factor variations and partial load," *IEEE Trans. Power Electron.,* vol. 30, no. 11, pp. 6320–6328, Nov. 2015.

[30] Q. Chen, L. Jiang, J. Hou, X. Ren and X. Ruan, "Research on bidirectional contactless resonant converter for energy charging between EVs," *in Proc. 39th Annu. Conf. IEEE Ind. Electron. Soc.,* Vienna, Nov. 2013, pp. 1236–1241.

[31] K. Colak, E. Asa, M. Bojarski, D. Czarkowski and O. C. Onar, "A novel phase-shift control of semibridgeless active rectifier for wireless power transfer," *IEEE Trans. Power Electron.,* vol. 30, no. 11, pp. 6288–6297, Nov. 2015.

[32] W. Gu and K. Harada, "A new method to regulate resonant converters," *IEEE Trans. Power Electron.,* vol. 3, no. 4, pp. 430–439, Oct. 1988.

[33] M. Yaqoob, K. Loo and Y. M. Lai, "Fully soft-switched dual-active-bridge series-resonant converter with switched-impedance-based power control," *IEEE Trans. Power Electron.,* vol. 33, no. 11, pp. 9267–9281, Nov. 2018.